

1
2
3
4
5
6
7
8
9
10
11
12
13
14
15
16
17
18
19
20
21
22
23
24
25
26
27
28
29
30
31
32
33
34
35
36
37
38
39
40
41
42
43
44
45
46
47
48
49
50
51
52
53
54
55
56
57
58
59
60

1
2
3 **Probing the Heterogeneity of Protein Kinase Activation in Cells by Super-Resolution**
4
5 **Microscopy.**
6
7

8
9 Ruobing Zhang^{†,‡,°,¶}, Gilbert O. Fruhwirth^{§,||,¶}, Oana Coban^{§,¶}, James E. Barrett[⊥], Thomas
10
11 Burgoyne[#], Sang Hak Lee^{†,‡}, Paul Dennis Simonson[†], Murat Baday^{‡,⊥,Δ}, Boris Kholodenko[∅],
12
13 Clare E. Futter[#], Tony Ng^{§,□,◇,*}, Paul R. Selvin^{†,‡,⊥,*}
14
15

16
17 [†] Department of Physics, [‡] Center for the Physics of Living Cells, and [⊥] Center for Biophysics
18 and Computational Biology, University of Illinois, 1110 West Green Street, Urbana, IL 61801,
19 USA.
20
21

22
23 [§] R. Dimpleby Department of Cancer Research, Randall Division of Cell and Molecular
24 Biophysics, Division of Cancer Studies, King's College London, Guy's Campus New Hunt's
25 House, London SE1 1UL, UK.
26
27

28
29 ^{||} Department of Imaging Chemistry and Biology, Division of Imaging Sciences and Biomedical
30 Engineering, St. Thomas' Hospital, King's College London, London SE1 7EH, UK.
31
32

33 [⊥] Department of Mathematics, King's College London, 25 Gordon Street, London WC2R 2LS,
34 UK.
35
36

37 [#] UCL Institute of Ophthalmology, 11-43 Bath Street, London EC1V 9EL, UK.
38

39 [∅] Systems Biology Ireland, Conway Inst. of Biomolecular & Biomedical Research, School of
40 Medicine and Medical Science, University College Dublin, Belfield, Dublin 4, Ireland.
41
42

43 [□] UCL Cancer Institute, Paul O'Gorman Building, University College London, London WC1E
44 6DD, UK.
45
46

47 [◇] Breakthrough Breast Cancer Research Unit, Department of Research Oncology, Guy's Hospital
48 King's College London School of Medicine, London SE1 9RT, UK.
49
50

51 Current addresses: [°] Department of Molecular and Cellular Biology, Harvard University,
52 Cambridge, 52 Oxford Street, MA 02138, USA; ^Δ Demirci Bio-Acoustic-MEMS in Medicine
53 Laboratory, School of Medicine, Stanford, CA94305, USA.
54
55

56
57 [¶] These authors contributed equally to this work.
58
59
60

* Correspondence by e-mail to tony.ng@kcl.ac.uk and selvin@illinois.edu.

1
2
3
4
5
6
7
8
9
10
11
12
13
14
15
16
17
18
19
20
21
22
23
24
25
26
27
28
29
30
31
32
33
34
35
36
37
38
39
40
41
42
43
44
45
46
47
48
49
50
51
52
53
54
55
56
57
58
59
60

ABSTRACT

Heterogeneity of mitogen-activated protein kinase (MAPK) activation in genetically identical cells, which occurs in response to epidermal growth factor receptor (EGFR) signaling, remains poorly understood. MAPK cascades integrate signals emanating from different EGFR spatial locations, including the plasma membrane and endocytic compartment. We previously hypothesized that in EGF-stimulated cells the MAPK phosphorylation (pMAPK) level and activity are largely determined by the spatial organization of the EGFR clusters within the cell. For experimental testing of this hypothesis, we used super-resolution microscopy to define EGFR clusters by receptor numbers (N) and average intra-cluster distances (d). From this data, we predicted the extent of pMAPK with 85% accuracy on a cell-to-cell basis with control data returning 54% accuracy ($P < 0.001$). For comparison, the prediction accuracy was only 61% ($P = 0.382$) when the diffraction-limited averaged fluorescence intensity/cluster was used. Large clusters ($N \geq 3$) with $d > 50\text{nm}$ were most predictive for pMAPK level in cells. Electron microscopy revealed that these large clusters were primarily localized to the limiting membrane of multivesicular bodies (MVB). Many tighter packed dimers/multimers ($d < 50\text{nm}$) were found on intraluminal vesicles within MVBs, where they were unlikely to activate MAPK because of the physical separation. Our results suggest that cell-to-cell differences in N and d contain crucial information to predict EGFR-activated cellular pMAPK levels and explain pMAPK heterogeneity in isogenic cells.

KEYWORDS

Cell-to-cell heterogeneity, EGFR, MAPK, super-resolution microscopy, Bayesian modeling.

1
2
3 In recent years it has become evident that an inhomogeneous microenvironment, combined with
4
5 the plasticity of the cancer genome, may lead to a significant degree of functional heterogeneity
6
7 amongst cancer cells of the same tumor.¹ The magnitude and timing of the output signal
8
9 commonly varies across a population of genetically identical cells.² The output signal integrates
10
11 various receptor inputs in space and time and directs important physiological processes such as
12
13 cell proliferation, migration and survival among cells in culture.³ Understanding the possible
14
15 ranges of cellular output heterogeneity and what contributes to them mechanistically would
16
17 represent a major leap forward in cell biology.
18
19
20
21

22
23 A particularly important example is the mitogen-activated protein kinase (MAPK) pathway,
24
25 which is a signaling hub for multiple cues and spatiotemporally organized intracellular signal
26
27 transmitters.⁴ Activation of MAPK signaling governs gene expression thereby controlling many
28
29 physiological processes.⁵ Overexpression of epidermal growth factor receptor (EGFR) has been
30
31 reported for a number of different tumor types.⁶ This has been postulated to lead to MAPK
32
33 activation by allowing the receptors on the cell membrane to randomly collide and interact with
34
35 one another with high frequency.⁷ Nanoscale imaging of the plasma membrane using near-field
36
37 scanning optical microscopy (NSOM) has recently shown that EGFR monomers are
38
39 preferentially organized in ~150nm clusters (*i.e.* not randomly distributed) in both untreated and
40
41 ligand-stimulated cells.⁸ Several other studies applied scanning force microscopy to quantify
42
43 EGFR clusters but have been restricted to monitoring their spatial organization only on the
44
45 plasma membrane.^{9,10} We previously hypothesized that the MAPK signaling activity is largely
46
47 determined by the spatial organization of the EGFR clusters (at a nanometer proximity scale),
48
49 which, together with the associated Shc/Grb2/SOS/RAS/RAF/MEK/MAPK complexes (that
50
51
52
53
54
55
56
57
58
59
60

1
2
3 usually involve assembling scaffold proteins), will mainly determine the MAPK signaling output
4
5 in individual cells.¹¹ Experimental validation of this hypothesis has not been achieved to date.
6
7

8
9 Nowadays super-resolution fluorescence imaging methods can achieve spatial resolutions in the
10
11 tens of nanometers.¹²⁻¹⁶ This enables the measurement of nanometer intra-cluster distances and
12
13 the number of receptor molecules per cluster throughout a mammalian cell which typically
14
15 spreads in the tens of micrometer range,¹⁷⁻¹⁹ identifying individual receptors and their clusters
16
17 located on various structural components. A prior study combined super-resolution microscopy
18
19 and single-molecule FRET to investigate the dynamics and localization of activated EGFR
20
21 dimers on the plasma membrane of live cells.²⁰ A different report applied STORM to provide
22
23 mechanistic insights into EGFR cluster formation.²¹ However, none of these studies has looked
24
25 at endocytosed EGFRs trafficking to multivesicular bodies (MVBs) located in the perinuclear
26
27 region of a cell.^{22,23} EGFR clusters continue to signal from the endosomal and MVB membranes,
28
29 activating MAPK *via* mechanisms that involve scaffold proteins such as MP1.²⁴⁻²⁶ Little is
30
31 known about the relationship between the cell-to-cell heterogeneity in the spatial organization of
32
33 these EGFR clusters and the functional consequences in the cellular response on a single cell
34
35 level.
36
37
38
39
40

41
42 Here, we used generalized single molecule high-resolution imaging with photobleaching
43
44 (gSHRIMP)^{12,15} to characterize the intra-cellular heterogeneity in MAPK phosphorylation levels
45
46 in response to EGF stimulation on a cell-by-cell basis. Quantum dot (QD) blinking has been
47
48 successfully used as an alternative to photoswitching of organic fluorophores or photo-
49
50 activatable proteins.²⁷ We quantified two EGFR cluster parameters, *i.e.* EGFR molecule number
51
52 per cluster (N) and average intra-cluster distance (d) between any two individual EGFR
53
54 molecules and used them as input parameters for a Bayesian model to predict MAPK signaling
55
56
57
58
59
60

1
2
3 output on a cellular basis. We also employed transmission electron microscopy (TEM) to
4
5 determine the spatial location of EGFR clusters in the cells relative to their organelle structures.
6
7 We were able to predict on a cell-by-cell level MAPK phosphorylation states on the basis of
8
9 nanoscale organizational differences in EGFR clusters that are super-resolved. This lends support
10
11 to and extends our previous proposition that the endosomal and MVB membrane localization of
12
13 EGFR clusters can cause an increase in the number (or average lifetime) of signaling complexes,
14
15 in a manner that is dependent on the spatial organization within the receptor oligomeric
16
17 configuration.¹¹
18
19
20
21
22
23
24
25
26
27
28
29
30
31
32
33
34
35
36
37
38
39
40
41
42
43
44
45
46
47
48
49
50
51
52
53
54
55
56
57
58
59
60

RESULTS AND DISCUSSION

Cell-to-cell heterogeneity in growth factor-stimulated MAPK phosphorylation. MAPK

(ERK1/ERK2) phosphorylation is a well-studied readout of MAPK pathway activation downstream of EGFR activation. We stimulated the monoclonal breast cancer cell line HCC1143 with EGF for various lengths of time at both 4°C and 37°C and analyzed MAPK phosphorylation on a population level by immunoblotting (see Supporting Information A, Fig. S1) and on a cell-by-cell level by immunofluorescence (Fig. 1). The antibodies we used were specific for the residues pT202/pY204 (ERK1) and pT185/pY187 (ERK2), respectively. Treatment at 4°C was used to engage receptors with EGF but slow signaling response and receptor endocytosis.²⁸ On a population basis, MAPK phosphorylation peaked after 15min of EGF treatment at 37°C (Fig. S1A-B). As expected, no MAPK phosphorylation was observed by treating cells at 4°C, although phosphorylation of EGFR, immediate adaptor proteins and some downstream targets (PI3K and PLC γ) at 15 and 30 min was previously reported.²⁹ Cellular heterogeneity of MAPK signaling was revealed by immunofluorescence microscopy after 15min or 30min treatment at 37°C, as is demonstrated by the broadening of the anti-pMAPK intensity distributions (Fig. 1). Full width half maximum (FWHM) was 138 arbitrary units (a.u.) when cells were treated at 4°C for 30min. FWHM increased to 524 a.u. after 15min at 37°C and narrowed upon longer treatment (30min at 37°C) to 336 a.u.; hence FWHM ratios (as a measure of histogram broadening) as compared to control conditions were 3.8 and 2.4, respectively. This shows an increase in range of observed pMAPK output values and reflects heterogenic behavior between these otherwise isogenic cells as compared to control conditions (4°C). It is noteworthy that averaging of immunofluorescence intensities over many cells led to a result resembling immunoblotting (Fig. S1C) as both techniques are averaging over the whole population.

1
2
3 Several studies reported on the existence of higher order ErbB multimers and their functional
4 relevance to signaling.³⁰⁻³² EGFR cluster formation has been reported to require EGFR kinase
5 activity.^{30,33} Members of the ErbB family have been shown to assemble into higher-order
6 nanostructures but precise structure-function relationship of these assemblies, in terms of how
7 they specify signal output, remains unclear.^{34,35} High-resolution imaging methods are required to
8 investigate the significance of receptor nanoscale organization in regulating its function. Ranges
9 of cluster diameters were measured with NSOM and found to have an average diameter of
10 150±80 nm EGF-stimulated HeLa cells.⁸ This study validated and complemented a prior report
11 that estimated an average EGFR cluster density of 33/μm² with 10–30 EGFR receptors per
12 cluster in the same cell line.³⁶

13
14
15
16
17
18
19
20
21
22
23
24
25
26
27
28
29
30 **Quantitative analysis of EGFR nanoclusters by super-resolution imaging.** We employed
31 super-resolution microscopy to visualize individual EGFR receptors and their oligomerization
32 patterns on the spatial scales below the diffraction limit following EGF stimulation.⁸ To
33 fluorescently label EGFR, we followed a previously reported approach³⁷ to generate equimolar
34 complexes of biotinylated EGF with streptavidin-QD565 (EBSQ) under carefully chosen
35 reaction conditions (see Methods). The EBSQ complex was verified to be equivalent with EGF
36 in stimulating pMAPK signaling responses and EGFR internalization (see Supporting
37 Information B, Fig. S2). The proximity between single EGFR molecules on the nanometer scale
38 has been recognized as a prerequisite for receptor activation, and crystallographic studies have
39 shown an asymmetric, ligand-induced activated EGFR dimer.^{38,39} Nanopositioning of EBSQ
40 molecules bound to EGFRs was based on the intrinsic capability of QDs to blink and was
41 determined using generalized SHRImP^{12,40} as described in Methods. Blinking was assigned to
42
43
44
45
46
47
48
49
50
51
52
53
54
55
56
57
58
59
60

1
2
3 individual QDs based on the observed step-wise intensity changes before and after blinking
4 events (Fig. 2A/D). Fig. 2 shows examples of an EGFR dimer (Fig. 2B/C) and an EGFR trimer
5 (Fig. 2E/F) including the corresponding intensity vs. time curves (Fig. 2A/D). The purple large
6 spot represents the diffraction-limited image of excited EGFRs bound to EBSQ molecules, while
7 the super-resolved individual EBSQ-bound EGFR positions are shown in white.
8
9

10
11
12
13
14
15
16 Our super-resolution technique (see Methods and Supporting Information C) allowed us to
17 resolve QDs with up to 15nm lateral resolution.¹² Here, the resolution is taken to be the smallest
18 distance at which two EGFR molecules could be separated. We estimated the EBSQ complexes
19 to be <20nm (see Supporting Information D). A cluster is defined as the group of super-resolved
20 receptors within a diffraction-limited spot. Intra-cluster distances (d_{ij}) were measured as
21 distances between individual QDs using centroid coordinates of each localized QD. In order to
22 correlate MAPK activation with EGFR cluster formation under different experimental
23 conditions, we measured first, MAPK phosphorylation of a cell using wide-field
24 immunofluorescence microscopy as a surrogate for its MAPK pathway activation and, second,
25 EGFR cluster organization by EBSQ super-resolution imaging. From the super-resolution
26 images we then determined the number of EGFR molecules per cluster (N) and the average intra-
27 cluster distance between EGFR monomers (d). When super-resolved, the vast majority of the
28 diffraction limited EBSQ spots imaged in HCC1143 cells incubated at 4°C were EGFR
29 monomers (>70%), with 20% EGFR dimers and the remainder being trimers and, rarely,
30 multimers (Fig. 3A). Upon EBSQ treatment at 37°C, this balance shifted dramatically at the
31 expense of EGFR monomers. Longer EBSQ stimulation at 37°C (30min) led to a reduction of
32 the number of dimers and trimers, but an increase in multimer numbers as compared to shorter
33 treatment (15min). This data is in line with previous reports of EGFR cluster formation upon
34
35
36
37
38
39
40
41
42
43
44
45
46
47
48
49
50
51
52
53
54
55
56
57
58
59
60

1
2
3 EGF treatment.^{33, 41} Some of the larger, multimeric clusters could not be spatially resolved and
4 hence, could not be included in the prediction of pMAPK based on d or N and d combined. A
5 number of clusters with N up to 4-6 were well resolved and included in the analysis (Fig. 3B).
6
7
8 For simplicity, from here onwards, we will refer to this particular cluster group as “ $N>3$ ”.

14 **Using the number of EGFR receptors per cluster (N) to predict cellular MAPK**

15
16 **phosphorylation.** Super-resolution microscopy allowed us to determine two important
17 parameters characterizing EGFR nanoclusters, N and d , which were used for a data-driven
18 prediction of the MAPK phosphorylation level as an indicator of EGFR signaling. To test
19 whether N or d , or both, contain any predictive information regarding the pMAPK intensity
20 levels, we used a mathematical model based on a Bayesian Linear Classifier (BLC).^{42,43} The
21 BLC is an algorithm that attempts to find a linear combination of input covariates that can be
22 used to predict which class each cell belongs to; classes were either ‘high/activated’ or
23 ‘low/resting’ MAPK phosphorylation. The pMAPK level was quantified by wide-field
24 immunofluorescence microscopy on a cell-by-cell basis by measuring the average fluorescence
25 intensity per unit area. Activated and resting cells separated in two groups that were significantly
26 different (Fig. 3C; $P<0.0001$), *i.e.* ‘high/activated’ or ‘low/resting’. The algorithm was first
27 trained to make a classification decision. The cells were randomly separated into a training set
28 and a validation set. Initially, the BLC was used to predict pMAPK using N as the only input
29 variable. The four covariates used were the fraction of monomers ($N=1$), dimers ($N=2$), trimers
30 ($N=3$) and oligomers ($N>3$) as determined by super-resolution microscopy for each individual
31 cell. Fig. 4A shows the training and validation success rates as a function of the number of
32 covariates used in the BLC with the corresponding weights shown in Fig. 4B. The trained BLC
33 predicted ‘high’ or ‘low’ MAPK phosphorylation classes using these input variables with an
34
35
36
37
38
39
40
41
42
43
44
45
46
47
48
49
50
51
52
53
54
55
56
57
58
59
60

1
2
3 accuracy of 65% ($P=0.090$) in the validation set. To compare, a randomized data set of no
4
5 predictive value yielded a prediction accuracy of 54%. Dimers and trimers were most predictive
6
7 for EGF-induced MAPK phosphorylation, shown by the positive weights (see Methods).
8
9

10
11 **Prediction of cellular MAPK phosphorylation is improved by inclusion of EGFR nanoscale**
12 **proximity information.** First, we tested if intra-cluster distances d alone contain any
13

14 information predictive for pMAPK. Applying BLC as before, we found d alone is not predictive
15
16 for pMAPK (46%; $P=0.733$; Supporting Information E; Fig. S4). We then combined both
17
18 parameters of EGFR cluster, N and d , to test if this would improve prediction accuracy as
19
20 compared to N alone. We divided the data into six subsets based on the various combinations
21
22 between the number of receptors per cluster ($N=2, 3, \text{ or } >3$) and average intra-cluster distance
23
24 ($d \leq 50\text{nm}$ or $d > 50\text{nm}$). Applying BLC with this new set of covariates, we achieved a prediction
25
26 accuracy of 85% ($P < 0.001$, Fig. 4C), which was much higher than what could be achieved with
27
28 either of the two parameters individually. Combination of $N=4$ and $N=3$ into one covariate
29
30 caused a drop in accuracy from 85% to 78% (the weight of the redefined covariate remains
31
32 positive and statistically significant). Thus, we upheld the previous division of subsets. The
33
34 probability of obtaining a ‘high’ MAPK phosphorylation classification in an individual cell was
35
36 observed to increase with increasing N until N became greater than 3 (Fig. 4A). The ranking of
37
38 the covariate weights of the intra-cluster distance (d) within the $N=3$ and $N>3$ clusters revealed
39
40 that $d > 50\text{nm}$ was positively correlated with a greater extent of MAPK phosphorylation (Fig. 4D;
41
42 $N=3$: $P=0.0465$, significant; $N>3$: $P=0.0601$, trend), *i.e.* trimers, and to a lesser extent, multimers
43
44 with an average intra-cluster distance $d > 50\text{nm}$ were the top predictive classes. In contrast,
45
46 clusters with $d \leq 50\text{nm}$ were not predictive for MAPK phosphorylation. The quantitative analysis
47
48 presented in Fig. 4 was performed on pooled data obtained from two independent biological
49
50
51
52
53
54
55
56
57
58
59
60

1
2
3 experiments for better statistics (individual experimental cohorts and their individual analyses
4
5 are shown in Supporting Information F). The two replicates displayed a similar distribution of
6
7 clusters across the covariate bins used (Fig. S5A) and achieved prediction accuracies of 89%
8
9 (Fig. S5B) and 82% (Fig. S5C), respectively.
10
11

12
13 It is noteworthy that the same BLC-based prediction of pMAPK could also be performed using
14
15 diffraction-limited fluorescence microscopy data. When we calculated the best achievable
16
17 predictive accuracy by using averaged fluorescence intensities of EGFR clusters per cell as the
18
19 only input, this resulted in a poor prediction accuracy of only 61% ($P=0.382$), which was
20
21 marginally above the randomized data set with no predictive value (54%).
22
23
24
25

26 Considering that nanoscale proximity between EGFR molecules is a prerequisite for EGFR
27
28 downstream signaling,^{38,39} our data appeared to be counter-intuitive. To find a possible
29
30 explanation why trimers and multimers with average intra-cluster distances $d>50\text{nm}$ are more
31
32 predictive than dimers, trimers and multimers with average intra-cluster distances $d\leq 50\text{nm}$ we
33
34 investigated the intracellular trafficking behavior of the EGFR sub-populations of interest by
35
36 direct visualization of their sub-cellular localization *via* TEM.
37
38
39
40

41 **Top predictive EGFR sub-populations localize predominantly on the limiting membrane of**
42
43 **MVBs.** To understand the relationship between the number of EGFRs per cluster N , the average
44
45 intra-cluster distance d and the BLC weighting of the super-resolution microscopy data, we
46
47 quantified the spatial distribution of clusters of $N=2$, $N=3$ and $N>3$ EGFR receptors and
48
49 correlated it to their location within endosomes as determined by TEM. TEM allowed us to
50
51 acquire images of sub-cellular structures and visualize the partitioning of individual and
52
53 clustered EGFRs between the limiting membranes of MVBs (Fig. S6) and ILVs within the MVB
54
55
56
57
58
59
60

1
2
3 lumen (Fig. 5A). The super-resolution approach analyses all EGFR regardless of position in the
4 cell while the requirement for ultra-high magnification to visualize gold by TEM prevents
5 parallel whole-cell analysis. We therefore only analyzed endocytosed EGFR gold particles
6
7
8
9
10 (present on small endocytic vesicles and MVBs with one or more ILVs), which also minimized
11 the possibility of analyzing EGFR that had not bound ligand. EGFR clusters were defined by all
12 gold labeled antibody-conjugated receptors with separation distances less than 22nm between
13 adjacent nanogold particles. The cut-off was empirically determined to sensibly assign particles
14 to a cluster as visualized in the TEM images. After 30 minutes at 37°C the majority of $N \geq 3$
15 multimers with larger intra-cluster distances displayed a tendency to localize on the limiting
16 membrane of MVBs (Fig. S6) whilst many of the more compact clusters were sequestered on
17 ILVs within the MVB lumen (Fig. 5B). The mean of the average size clusters with $N \geq 3$ located
18 on the limiting membrane was significantly larger than that of clusters located on ILVs
19
20
21
22
23
24
25
26
27
28
29
30
31
32
33
34
35
36
37
38
39
40
41
42
43
44
45
46
47
48
49
50
51
52
53
54
55
56
57
58
59
60

($P=0.0247$, unpaired two-tailed t -test with Welch's correction). This is a good fit with our model showing that EGFR trimer and multimer subpopulations with large intra-cluster distances ($N \geq 3$, $d > 50\text{nm}$) are top predictors of MAPK phosphorylation.

We found the most predictive EGFR subpopulation to be $N \geq 3$ clusters with average sizes larger than 50nm ($P=0.0465$). This first appeared counter-intuitive considering EGFR signaling is initiated upon ligand binding to the receptor followed by its dimerization/multimerization. Importantly, TEM experiments allowed us to reveal the sub-cellular organization of the various subpopulations. While TEM does not have the quantitative statistical power of the super-resolution approach, it reveals the suborganellar EGFR distribution. TEM suggests a possible explanation for the predictive power of larger clusters ($N \geq 3$, $d > 50\text{nm}$) compared with smaller clusters. The predictive large clusters were mainly located on the limiting membrane of

1
2
3 endocytic vesicles and multivesicular bodies where they play an active role in signal
4
5 transduction. In contrast, many dimers and densely packed EGFR multimers ($N \geq 3$, $d \leq 50\text{nm}$)
6
7 were located on ILVs and thus, no longer contributed to the overall EGFR signaling response
8
9 because of their physical separation from the vast majority of the MAPK pool, which resides in
10
11 the cytosol.
12
13

14
15
16 The significance of the EGFR ≥ 3 multimers on the limiting membrane in triggering the MAPK
17
18 signaling output may be explained by virtue of the associated Shc/Grb2/SOS/RAS/RAF/MEK/
19
20 MAPK complexes as we previously postulated through models.¹¹ Some corroborative evidence
21
22 for this has previously been obtained using image correlation spectroscopy and Foerster
23
24 resonance energy transfer imaging. This approach showed in EGF-stimulated BaF/3 cells that
25
26 were stably transfected with Grb2 (Grb2-mRFP) and EGFR (EGFR-eGFP), nanometer-scale
27
28 association of Grb2-mRFP with EGFR-eGFP multimers, which contained, on average, 4 ± 1
29
30 copies of EGFR-eGFP.⁴⁴ Many differences exist between this observation and our current work.
31
32 These include differences in cell types, overexpressed⁴⁵ vs. endogenous receptors (our study).
33
34 Importantly, both report on a similar stoichiometry of the EGFR multimers that signal most
35
36 efficiently in cells.
37
38
39
40
41
42

43
44 The spatial organization of cell surface receptors on variable length scales (from molecules to
45
46 micrometers) plays an important role in cell signaling.⁴⁵ These cell-to-cell differences can
47
48 provide a mechanism to control protein interactions and thus modulate signal transduction
49
50 efficiency. Here, we were able to relate the spatial organization of the EGFR receptors to
51
52 signaling dynamics and show that large EGFR trimers are the most predictive subpopulation for
53
54 MAPK phosphorylation output. Our results strengthen the hypothesis that supramolecular
55
56 receptor organization and spatial compartmentalization play a decisive role in signal
57
58
59
60

1
2
3 transduction, thereby influencing cell fate and function. Our findings further reveal EGFR
4 trimers and their intra-cluster distances to play a role as a marker of MAPK phosphorylation.
5
6 Pending further validation in more complex samples such as cell mixtures and tissues, this
7
8 finding has potential applications beyond mechanistic signal transduction studies. A better
9
10 understanding of the role of differentially located EGFR multimers (limiting membrane *vs.* ILV),
11
12 *e.g.* by further dissecting the *N* & *d* information of our reported ILV-located EGFR in the context
13
14 of chemotherapy resistance,⁴⁶ may have potential value in future clinical applications.
15
16
17
18
19
20
21
22
23
24
25
26
27
28
29
30
31
32
33
34
35
36
37
38
39
40
41
42
43
44
45
46
47
48
49
50
51
52
53
54
55
56
57
58
59
60

CONCLUSION

To better understand how signals are integrated and transmitted through signaling networks, we provide a framework for using super-resolution microscopy to access detailed spatial information about specific cellular molecules, and how to use it, in combination with mathematical modeling, to predict cellular outcomes. As a paradigm, we focused on how the spatial organization of the EGFR oligomeric network specifies the output signal through to MAPK phosphorylation in genetically identical cells. Ensemble behaviors of a population of cells may not reveal silent features of cell signaling. On the other hand, cell-to-cell differences are always present in any cell population and may or may not serve a biological function or contain meaningful information. Super-resolution imaging has been previously combined with TEM,¹³ but we report here an integrated cell-by-cell approach between the two imaging techniques to extract detailed spatial information on EGFR distribution. Assembly of EGFRs into homodimers and small size multimers occurs on spatial scales in between those probed by FRET (<10nm) and diffraction-limited microscopy (>200nm). Our method, with a resolution of 15nm, is an excellent approach for studying receptor multimerization at this spatial scale.

Our approach was to analyze and interpret heterogeneity in cellular pMAPK levels by looking at the individual cell behavior and correlating it to the detailed spatial organization of super-resolved EGFR clusters. Our finding is that the number of EGFR molecules per cluster N and the average EGFR intra-cluster distance d are highly informative for the prediction of the EGF-driven pMAPK output. N alone, d alone, and N and d combined were alternatively used as input parameters for a BLC to model, train and validate the technique resulting in prediction accuracies for MAPK phosphorylation of 65% ($P=0.090$), 46% ($P=0.733$) and 85% ($P<0.001$), respectively. A randomized data set of no predictive value yielded an accuracy of 54%,

1
2
3 demonstrating a 31% gain in accuracy if the *N and d* information is combined. The intra-cluster
4 distance information is crucial in this prediction as it improves accuracy from 65% ($P=0.090$;
5 with only EGFR numbers regarded) to 85% ($P<0.001$). We and others have previously applied
6 super-resolution imaging to visualize EGFR clusters.^{20,21,27} Here we report using super-resolved
7 cluster parameters to accurately predict the individual cells' MAPK phosphorylation levels. This
8 approach of combining advanced imaging with mathematical modeling to understand systems
9 level integration can be extended to improve our understanding of how many similar receptor
10 tyrosine kinases function in various types of cancer.
11
12
13
14
15
16
17
18
19
20
21
22
23
24
25
26
27
28
29
30
31
32
33
34
35
36
37
38
39
40
41
42
43
44
45
46
47
48
49
50
51
52
53
54
55
56
57
58
59
60

METHODS

Reagents. 565nm Streptavidin-coated quantum dots (QD) and biotinylated EGF (Life Technologies). Mouse anti-phospho p42/44 MAPK (clone MAPK-YT) antibody (Sigma). Mouse anti-phospho p42/44-ERK1/2 and rabbit anti total-ERK1/2 antibodies (Cell Signaling Technologies). Mouse monoclonal anti-EGFR antibody clone F4 binding to the sequence DVVDADADEYLIPQ, which corresponds to EGFR amino acid residues 985-996, was obtained from the monoclonal antibody facility at Cancer Research UK. Donkey anti-mouse secondary antibodies conjugated to either DyLight594 or Cy2 (Jackson Immuno Research) and goat anti-mouse-HRP and goat anti-rabbit-HRP secondary antibodies (Dako). Unconjugated EGF (Peprotech). SpheroTM polystyrene beads (average diameter 1.23 μ m, Spherotech). Mowiol (Polysciences). All standard chemicals (Sigma-Aldrich or VWR).

Cell treatments and sample preparation for super-resolution microscopy. 30,000 triple-negative HCC1143 (ATCC) cells/cm² were seeded in complete 10% FBS-containing growth medium (RPMI 1640 supplemented with 4.5g/L glucose, 25mM *L*-glutamine and 100IU penicillin/streptomycin) onto sterile acid-treated glass coverslips (20mm diameter, glass thickness No.1.5; Metzler). On the day of the experiment, cells were washed twice with serum-free growth medium and then treated with 10nM pre-formed EGF-biotin:streptavidin-QD565 (EBSQ) complexes in serum-free growth medium at either 4°C or 37°C for the indicated times. EBSQ complexes were formed by mixing equimolar amounts of pre-washed streptavidin-QD565 with biotinylated EGF (both from Life Technologies). A dilute solution of biotinylated EGF (200nM) was slowly pipetted using a Hamilton syringe (over minutes) into a more concentrated solution of streptavidin-QD565 (1 μ M) while continuously stirring. The mixture was allowed to react for 30min on ice. The equimolar reaction was carried out at a biotin:streptavidin ratio of

1
2
3 1:16-20. Reaction mixtures were purified from potential free EGF using P30 size exclusion spin
4
5 columns (Biorad). After treatment, cells were washed three times with ice-cold Tris-buffered
6
7 saline (TBS; 25mM Tris/HCl, 150mM NaCl, pH=7.4) and fixed for 15min in 4% (w/v) freshly
8
9 prepared paraformaldehyde (PFA) dissolved in TBS. Subsequently, cells were permeabilized
10
11 with 0.4% (v/v) Triton X-100 in TBS, washed twice with TBS, and blocked with 1% (w/v)
12
13 bovine serum albumin (BSA) in TBS for 20min at room temperature. Cells were then incubated
14
15 with the indicated primary antibodies (in blocking solution, at 4°C for 16h), washed three times
16
17 with TBS and then stained with the indicated secondary antibodies in blocking solution at room
18
19 temperature for 45min. After two washing steps each with TBS and distilled water, samples were
20
21 mounted in Mowiol (Polysciences) and left to air dry in the dark at room temperature overnight.
22
23 To correct for stage drift, polystyrene beads (0.1% (w/v), average diameter 1.23µm, Spherotech)
24
25 were added to the mounting medium as fiduciary markers.
26
27
28
29
30
31

32
33 **Confocal fluorescence microscopy.** Confocal images were obtained using an upright Zeiss
34
35 LSM 510 META confocal microscope, equipped with a blue 405 diode laser, an argon ion laser
36
37 and a green HeNe 543nm laser using the recommended filter sets for imaging of Hoechst 33342,
38
39 FITC/GFP, and TRITC/RFP. Images were taken with a Plan-Apochromat oil objective 63×
40
41 NA=1.4 (Zeiss). Image processing was performed using the Fiji/ImageJ software.
42
43
44

45
46 **gSHRImP super-resolution imaging with QD blinking.** Super-resolution images were
47
48 acquired using gSHRImP mostly as previously reported.^{12,15} Here, specifically, intrinsic blinking
49
50 of quantum dots instead of photobleaching of organic dyes was employed to achieve super-
51
52 resolution. We used backward subtraction of the image frames to find single blinking events of
53
54 individual QDs and stochastically resolve their localizations with nanometer accuracy. Drift
55
56 correction (Fig. S3) was performed using bright-field scattering images of the non-fluorescent
57
58
59
60

1
2
3 beads acquired on a distinct CCD camera (CV-A55 IR E, JAI Ltd.) synchronized to the
4
5 fluorescence imaging CCD (iXon+, Andor) for the entire duration of the measurement. Images
6
7 were acquired at a rate of 33 frames/s. Typically, we imaged areas with a minimum of three
8
9 fluorescent beads in the field of view and plotted the calibration drift curve by averaging the
10
11 beads displacement in the x and y direction, respectively. Trajectories were extracted by tracking
12
13 the beads position at each frame using in-house written code running on the IDL platform
14
15 version 8.4 (Exelis). All images were corrected for drift individually and super-resolution images
16
17 were plotted using in-house written software as previously reported.¹⁵
18
19
20
21
22

23 **Sample preparation for transmission electron microscopy (TEM).** 300,000 HCC1143

24
25 cells/cm² were seeded on 6-well Epon plates (Agar Scientific) in serum-containing growth
26
27 medium. On the next day, cells were washed twice with serum-free growth medium before they
28
29 were incubated with the anti-EGFR antibody directed against the extracellular EGFR domain
30
31 (clone 108) that was conjugated to colloidal 10nm gold particles as previously described.⁴⁷
32
33 Optimum gold loading into the cells was observed for 30min incubation with 80nM EGF
34
35 (Peprotech) present alongside the gold-conjugated EGFR antibody. Subsequently, cells were
36
37 fixed by applying a mixture of 2% (w/v) PFA and 2% (v/v) glutaraldehyde in 0.1M cacodylate
38
39 buffer for 30min. After washing twice with 0.1M cacodylate buffer, cells were treated with 1%
40
41 tannic acid in cacodylate buffer and prepared for TEM as previously reported⁴⁸. Sections of
42
43 70nm thickness were cut using a Leica EM UC microtome and imaged on a JEOL JEM 1010
44
45 electron microscope.
46
47
48
49
50

51
52 **Cluster analysis of TEM data.** EGFR cluster analysis was done using Fiji/ImageJ software with
53
54 the Graph plugin.⁴⁹ Gold particles were manually selected and the distance matrix between all
55
56 the particles was calculated. Adjacent particles separated by less than 50nm between their
57
58
59
60

1
2
3 centroids were classified as connected components and assigned to the same cluster. The number
4
5 of particles per cluster (N_{EM}) and the average intra-cluster distance (d_{EM}) were determined for a
6
7 total of 10 cells and 702 clusters. The average intra-cluster distance was calculated as the average
8
9 of all distances between all particles within the cluster.
10
11

12
13 **Bayesian Linear Classifier analysis.** A Bayesian Linear Classifier (BLC)⁴³ was used to predict
14
15 MAPK activation status on a cell-by-cell basis. Cells were assigned to a 'high' or 'low' binary
16
17 class depending on MAPK phosphorylation (fluorescence intensity averaged over the entire cell).
18
19 The fluorescence intensity was calculated from a single frame, right after the exposure to the
20
21 excitation light and before any photobleaching could occur. The threshold for separating the two
22
23 classes represented the halfway value between the medians of the EGF treated and untreated cell
24
25 populations, and was determined to be 2396 a.u. A cell belonged to the 'high' class if its average
26
27 fluorescence intensity per pixel was higher, and to the 'low' class if lower, than the threshold
28
29 value. MAPK phosphorylation prediction was based on the various covariates derived from
30
31 super-resolution imaging of EGFR clusters, *i.e.* proportions of clusters in each of the N -mer or N -
32
33 d subclasses. The BLC seeks an optimal linear relationship between the input parameters and the
34
35 binary classes. The intra-cohort reproducibility of the BLC classification was estimated using
36
37 Leave One Out (LOO) Cross Validation. One sample is set aside for validation and the
38
39 remaining samples are used for training the BLC. The cells were randomly separated into a
40
41 training set and a validation set (see Methods); the training set was used to train the BLC, which
42
43 subsequently was used for predictions using the validation set. The BLC was first used with a
44
45 complete set of input variables, then the least informative covariate was removed (the one with
46
47 the smallest weighting) and a new BLC was trained and used for prediction. Once trained, the
48
49 model was used to predict which class the omitted sample belonged to. This was repeated until
50
51
52
53
54
55
56
57
58
59
60

1
2
3 each sample in the cohort had been used for validation. The training success was defined as the
4
5 (mean) fraction of cells correctly classified after training and the validation success was the
6
7 fraction of validation set cells that were correctly predicted. The BLC assigned weights to each
8
9 of the input parameters. These indicate the relative strength of each parameter as a reporter of
10
11 EGFR signaling to MAPK. The weights are determined by computing the maximum *a posteriori*
12
13 (MAP) solution of the BLC. To obtain 95% Credible Intervals (CI) we approximated the
14
15 posterior density with a multivariate Gaussian density by evaluating the curvature matrix at the
16
17 MAP solution. By making predictions on a validation dataset we tested the reproducibility of the
18
19 inferred weights. The high validation performance indicates that the inferred weights are genuine
20
21 (as opposed to statistical flukes). Beginning with all of the covariates, the covariate with the
22
23 smallest absolute value weight (averaged over training and validation runs) was eliminated and
24
25 the entire procedure was repeated until only a single covariate remained. Under the null
26
27 hypothesis that there is no association between the covariates and high/low intensity status we
28
29 estimated a *P* value using a permutation test. The covariates were randomly permuted 1000 times
30
31 and the maximum prediction accuracy was recorded each time. A *P* value was obtained based on
32
33 the comparison of the observed predictive accuracy with a randomized data set of no predictive
34
35 value (that yielded a prediction accuracy of 54%).
36
37
38
39
40
41
42
43
44
45
46
47
48
49
50
51
52
53
54
55
56
57
58
59
60

ACKNOWLEDGEMENT

The Selvin lab (PRS, RZ, SHL, PDS and MB) was supported by NIH GM108578 and NSF DBI 10-63188 and PHY-1430124. TN is supported by an endowment fund from Dimpleby Cancer Care to King's College London. Additional funding was provided by the KCL-UCL Comprehensive Cancer Imaging Centre (CCIC), CR-UK & EPSRC in association with the MRC and DoH (England) (GF, OC and JB), as well as a BBSRC Programme grant (OC). J. Barrett was also supported by a European Union FP7 grant (IMAGINT, 259881). The Futter lab (CF and TB) is supported by the Wellcome Trust (093445).

SUPPORTING INFORMATION AVAILABLE

This material is available free of charge *via* the Internet at <http://pubs.acs.org>. We provide supporting information including: (A) the analysis of population-based MAPK phosphorylation in response to EGF; (B) the validation of the EBSQ complex as compared to EGF; (C) details about super-resolution achieved by QD blinking; (D) a size estimation of the EBSQ complex; (E) that intra-cluster distances d in isolation are not predictive for MAPK phosphorylation; (F) the BLC-based pMAPK prediction for both individual experimental cohorts; and (G) a representative transmission electron microscopy image showing EGFR clusters at the limiting membrane of multivesicular bodies.

REFERENCES

- 1
2
3
4
5
6 (1) Gerlinger, M.; Rowan, A. J.; Horswell, S.; Larkin, J.; Endesfelder, D.; Gronroos, E.;
7 Martinez, P.; Matthews, N.; Stewart, A.; Tarpey, P.; Varela, I.; Phillimore, B.; Begum, S.;
8 McDonald, N. Q.; Butler, A.; Jones, D.; Raine, K.; Latimer, C.; Santos, C. R.; Nohadani, M. *et*
9 *al.*, Intratumor Heterogeneity and Branched Evolution Revealed by Multiregion Sequencing. *N*
10 *Engl J Med* **2012**, *366*, 883-892.
- 11 (2) Spencer, S. L.; Gaudet, S.; Albeck, J. G.; Burke, J. M.; Sorger, P. K., Non-Genetic
12 Origins of Cell-to-Cell Variability in Trail-Induced Apoptosis. *Nature* **2009**, *459*, 428-432.
- 13 (3) Spencer, S. L.; Sorger, P. K., Measuring and Modeling Apoptosis in Single Cells. *Cell*
14 **2011**, *144*, 926-939.
- 15 (4) Kholodenko, B. N., Map Kinase Cascade Signaling and Endocytic Trafficking: A
16 Marriage of Convenience? *Trends Cell Biol* **2002**, *12*, 173-177.
- 17 (5) Chang, L.; Karin, M., Mammalian Map Kinase Signalling Cascades. *Nature* **2001**, *410*,
18 37-40.
- 19 (6) Nicholson, R. I.; Gee, J. M.; Harper, M. E., Egfr and Cancer Prognosis. *Eur J Cancer*
20 **2001**, *37 Suppl 4*, S9-15.
- 21 (7) Orton, R. J.; Adriaens, M. E.; Gormand, A.; Sturm, O. E.; Kolch, W.; Gilbert, D. R.,
22 Computational Modelling of Cancerous Mutations in the Egfr/Erk Signalling Pathway. *BMC Syst*
23 *Biol* **2009**, *3*, 100.
- 24 (8) Abulrob, A.; Lu, Z.; Baumann, E.; Vobornik, D.; Taylor, R.; Stanimirovic, D.; Johnston,
25 L. J., Nanoscale Imaging of Epidermal Growth Factor Receptor Clustering: Effects of Inhibitors.
26 *J Biol Chem* **2010**, *285*, 3145-3156.
- 27 (9) Ianoul, A.; Street, M.; Grant, D.; Pezacki, J.; Taylor, R. S.; Johnston, L. J., Near-Field
28 Scanning Fluorescence Microscopy Study of Ion Channel Clusters in Cardiac Myocyte
29 Membranes. *Biophys J* **2004**, *87*, 3525-3535.
- 30 (10) Harootunian, A.; Betzig, E.; Isaacson, M.; Lewis, A., Super-Resolution Fluorescence
31 near-Field Scanning Optical Microscopy *Applied Physics Letters* **1986**, *49*, 674-676.
- 32 (11) Kholodenko, B. N., Four-Dimensional Organization of Protein Kinase Signaling
33 Cascades: The Roles of Diffusion, Endocytosis and Molecular Motors. *J Exp Biol* **2003**, *206*,
34 2073-2082.
- 35 (12) Gordon, M. P.; Ha, T.; Selvin, P. R., Single Molecule High Resolution Imaging with
36 Photobleaching. *Proceedings of National Academy of Science* **2004**, *101*, 6462-6465.
- 37 (13) Betzig, E.; Patterson, G. H.; Sougrat, R.; Lindwasser, O. W.; Olenych, S.; Bonifacino, J.
38 S.; Davidson, M. W.; Lippincott-Schwartz, J.; Hess, H. F., Imaging Intracellular Fluorescent
39 Proteins at Nanometer Resolution. *Science* **2006**, *313*, 1642-1645.
- 40 (14) Bates, M.; Huang, B.; Dempsey, G. T.; Zhuang, X., Multicolor Super-Resolution
41 Imaging with Photo-Switchable Fluorescent Probes. *Science* **2007**, *317*, 1749-1753.
- 42 (15) Simonson, P. D.; Rothenberg, E.; Selvin, P. R., Single-Molecule-Based Super-Resolution
43 Imaging in the Presence of Multiple Fluorophores. *Nano Lett* **2011**, *11*, 5090-5096.
- 44 (16) Wildanger, D.; Medda, R.; Kastrop, L.; Hell, S. W., A Compact Sted Microscope
45 Providing 3d Nanoscale Resolution. *J Microsc* **2009**, *236*, 35-43.
- 46 (17) Patterson, G.; Davidson, M.; Manley, S.; Lippincott-Schwartz, J., Superresolution
47 Imaging Using Single-Molecule Localization. *Annu Rev Phys Chem* **2010**, *61*, 345-367.
- 48 (18) Sahl, S. J.; Moerner, W. E., Super-Resolution Fluorescence Imaging with Single
49 Molecules. *Curr Opin Struct Biol* **2013**, *23*, 778-787.
- 50
51
52
53
54
55
56
57
58
59
60

1
2
3 (19) Lee, H. L.; Lord, S. J.; Iwanaga, S.; Zhan, K.; Xie, H.; Williams, J. C.; Wang, H.;
4 Bowman, G. R.; Goley, E. D.; Shapiro, L.; Twieg, R. J.; Rao, J.; Moerner, W. E.,
5 Superresolution Imaging of Targeted Proteins in Fixed and Living Cells Using Photoactivatable
6 Organic Fluorophores. *J Am Chem Soc* **2010**, *132*, 15099-15101.

7
8 (20) Winckler, P.; Lartigue, L.; Giannone, G.; De Giorgi, F.; Ichas, F.; Sibarita, J. B.; Lounis,
9 B.; Cognet, L., Identification and Super-Resolution Imaging of Ligand-Activated Receptor
10 Dimers in Live Cells. *Sci Rep* **2013**, *3*, 2387.

11 (21) Gao, J.; Wang, Y.; Cai, M.; Pan, Y.; Xu, H.; Jiang, J.; Ji, H.; Wang, H., Mechanistic
12 Insights into Egrf Membrane Clustering Revealed by Super-Resolution Imaging. *Nanoscale*
13 **2015**, *7*, 2511-2519.

14 (22) Eden, E. R.; White, I. J.; Tsapara, A.; Futter, C. E., Membrane Contacts between
15 Endosomes and Er Provide Sites for Ptp1b-Epidermal Growth Factor Receptor Interaction. *Nat*
16 *Cell Biol* **2010**, *12*, 267-272.

17 (23) Futter, C. E.; Pearse, A.; Hewlett, L. J.; Hopkins, C. R., Multivesicular Endosomes
18 Containing Internalized Egf-Egf Receptor Complexes Mature and Then Fuse Directly with
19 Lysosomes. *J Cell Biol* **1996**, *132*, 1011-1023.

20 (24) Eden, E. R.; Huang, F.; Sorkin, A.; Futter, C. E., The Role of Egf Receptor
21 Ubiquitination in Regulating Its Intracellular Traffic. *Traffic* **2012**, *13*, 329-337.

22 (25) Taub, N.; Teis, D.; Ebner, H. L.; Hess, M. W.; Huber, L. A., Late Endosomal Traffic of
23 the Epidermal Growth Factor Receptor Ensures Spatial and Temporal Fidelity of Mitogen-
24 Activated Protein Kinase Signaling. *Mol Biol Cell* **2007**, *18*, 4698-4710.

25 (26) Ceresa, B. P., Spatial Regulation of Epidermal Growth Factor Receptor Signaling by
26 Endocytosis. *Int J Mol Sci* **2012**, *14*, 72-87.

27 (27) Wang, Y.; Fruhwirth, G.; Cai, E.; Ng, T.; Selvin, P. R., 3d Super-Resolution Imaging
28 with Blinking Quantum Dots. *Nano Lett* **2013**, *13*, 5233-5241.

29 (28) Ng, T.; Shima, D.; Squire, A.; Bastiaens, P. I.; Gschmeissner, S.; Humphries, M. J.;
30 Parker, P. J., Pkcalpha Regulates Beta1 Integrin-Dependent Cell Motility through Association
31 and Control of Integrin Traffic. *EMBO J* **1999**, *18*, 3909-3923.

32 (29) Moehren, G.; Markevich, N.; Demin, O.; Kiyatkin, A.; Goryanin, I.; Hoek, J. B.;
33 Kholodenko, B. N., Temperature Dependence of the Epidermal Growth Factor Receptor
34 Signaling Network Can Be Accounted for by a Kinetic Model. *Biochemistry* **2002**, *41*, 306-320.

35 (30) Clayton, A. H.; Walker, F.; Orchard, S. G.; Henderson, C.; Fuchs, D.; Rothacker, J.;
36 Nice, E. C.; Burgess, A. W., Ligand-Induced Dimer-Tetramer Transition During the Activation
37 of the Cell Surface Epidermal Growth Factor Receptor-a Multidimensional Microscopy
38 Analysis. *J Biol Chem* **2005**, *280*, 30392-30399.

39 (31) Nagy, P.; Claus, J.; Jovin, T. M.; Arndt-Jovin, D. J., Distribution of Resting and Ligand-
40 Bound Erbb1 and Erbb2 Receptor Tyrosine Kinases in Living Cells Using Number and
41 Brightness Analysis. *Proc Natl Acad Sci U S A* **2010**, *107*, 16524-16529.

42 (32) Yang, S.; Raymond-Stintz, M. A.; Ying, W.; Zhang, J.; Lidke, D. S.; Steinberg, S. L.;
43 Williams, L.; Oliver, J. M.; Wilson, B. S., Mapping Erbb Receptors on Breast Cancer Cell
44 Membranes During Signal Transduction. *J Cell Sci* **2007**, *120*, 2763-2773.

45 (33) Hofman, E. G.; Bader, A. N.; Voortman, J.; van den Heuvel, D. J.; Sigismund, S.;
46 Verkleij, A. J.; Gerritsen, H. C.; van Bergen en Henegouwen, P. M., Ligand-Induced Egf
47 Receptor Oligomerization Is Kinase-Dependent and Enhances Internalization. *J Biol Chem* **2010**,
48 *285*, 39481-39489.

1
2
3 (34) Wang, J.; Yu, X.; Boriskina, S. V.; Reinhard, B. M., Quantification of Differential ErbB1
4 and ErbB2 Cell Surface Expression and Spatial Nanoclustering through Plasmon Coupling. *Nano*
5 *Lett* **2012**, *12*, 3231-3237.

6
7 (35) Yarden, Y.; Sliwkowski, M. X., Untangling the ErbB Signalling Network. *Nat Rev Mol*
8 *Cell Biol* **2001**, *2*, 127-137.

9 (36) Clayton, A. H.; Tavarnesi, M. L.; Johns, T. G., Unligated Epidermal Growth Factor
10 Receptor Forms Higher Order Oligomers within Microclusters on A431 Cells That Are Sensitive
11 to Tyrosine Kinase Inhibitor Binding. *Biochemistry* **2007**, *46*, 4589-4597.

12 (37) Lidke, D. S.; Nagy, P.; Heintzmann, R.; Arndt-Jovin, D. J.; Post, J. N.; Grecco, H. E.;
13 Jares-Erijman, E. A.; Jovin, T. M., Quantum Dot Ligands Provide New Insights into ErbB/Her
14 Receptor-Mediated Signal Transduction. *Nat Biotechnol* **2004**, *22*, 198-203.

15 (38) Jura, N.; Endres, N. F.; Engel, K.; Deindl, S.; Das, R.; Lamers, M. H.; Wemmer, D. E.;
16 Zhang, X.; Kuriyan, J., Mechanism for Activation of the EGF Receptor Catalytic Domain by the
17 Juxtamembrane Segment. *Cell* **2009**, *137*, 1293-1307.

18 (39) Zhang, X.; Gureasko, J.; Shen, K.; Cole, P. A.; Kuriyan, J., An Allosteric Mechanism for
19 Activation of the Kinase Domain of Epidermal Growth Factor Receptor. *Cell* **2006**, *125*, 1137-
20 1149.

21 (40) Zhang, R.; Rothenberg, E.; Fruhwirth, G.; Simonson, P. D.; Ye, F.; Golding, I.; Ng, T.;
22 Lopes, W.; Selvin, P. R., Two-Photon 3D Imaging of Individual Quantum Dots in an Aqueous
23 Environment. *Nano Lett* **2011**, *11*, 4074-4078.

24 (41) Ariotti, N.; Liang, H.; Xu, Y.; Zhang, Y.; Yonekubo, Y.; Inder, K.; Du, G.; Parton, R. G.;
25 Hancock, J. F.; Plowman, S. J., Epidermal Growth Factor Receptor Activation Remodels the
26 Plasma Membrane Lipid Environment to Induce Nanocluster Formation. *Mol Cell Biol* **2010**, *30*,
27 3795-3804.

28 (42) Barrett, J., Bayesian Linear Classifier.
29 <http://www.mathworks.com/matlabcentral/fileexchange/44472-bayesian-linear-classifier> **25 Nov**
30 **2013**.

31 (43) Chang, C. C.; Lin, C. J., Training Nu-Support Vector Classifiers: Theory and Algorithms.
32 *Neural Comput* **2001**, *13*, 2119-2147.

33 (44) Kozer, N.; Barua, D.; Henderson, C.; Nice, E. C.; Burgess, A. W.; Hlavacek, W. S.; Clayton, A.
34 H. A., Recruitment of the Adaptor Protein Grb2 to EGF Tetramers. *Biochemistry* **2014**, *53*, 2594-2604.

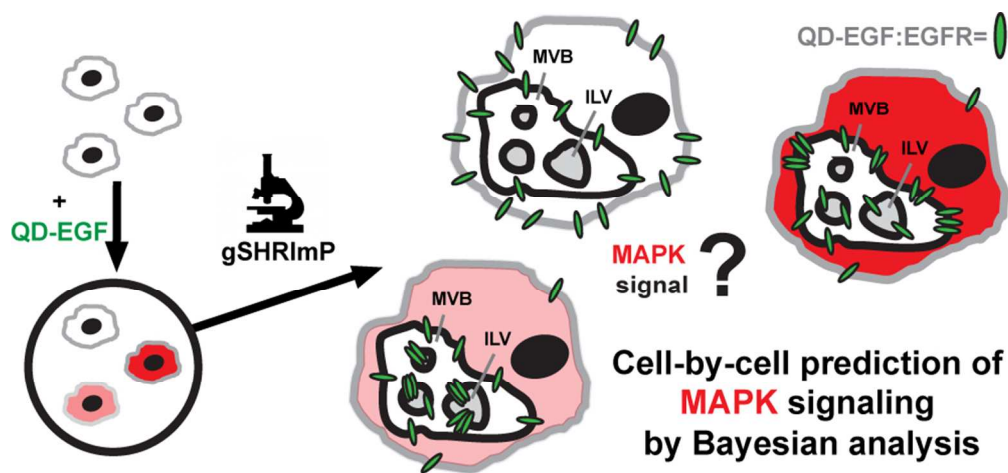
35 (45) Manz, B. N.; Jackson, B. L.; Petit, R. S.; Dustin, M. L.; Groves, J., T-Cell Triggering
36 Thresholds Are Modulated by the Number of Antigen within Individual T-Cell Receptor
37 Clusters. *Proc Natl Acad Sci U S A* **2011**, *108*, 9089-9094.

38 (46) Tomas, A.; Vaughan, S. O.; Burgoyne, T.; Sorkin, A.; Hartley, J. A.; Hochhauser, D.;
39 Futter, C. E., Wash and Tsg101/Alix-Dependent Diversion of Stress-Internalized EGF from the
40 Canonical Endocytic Pathway. *Nat Commun* **2015**, *6*, 7324.

41 (47) Slot, J. W.; Geuze, H. J., A New Method of Preparing Gold Probes for Multiple-Labeling
42 Cytochemistry. *Eur J Cell Biol* **1985**, *38*, 87-93.

43 (48) Stinchcombe, J. C.; Nomoto, H.; Cutler, D. F.; Hopkins, C. R., Anterograde and
44 Retrograde Traffic between the Rough Endoplasmic Reticulum and the Golgi Complex. *J Cell*
45 *Biol* **1995**, *131*, 1387-1401.

46 (49) Tupper, B., Image J Graph Plugin (version 2010/08/31).
47 <http://rsbweb.nih.gov/ij/plugins/graph>, accessed on 2012/04/23.



Graphic Table of Content

84x39mm (300 x 300 DPI)

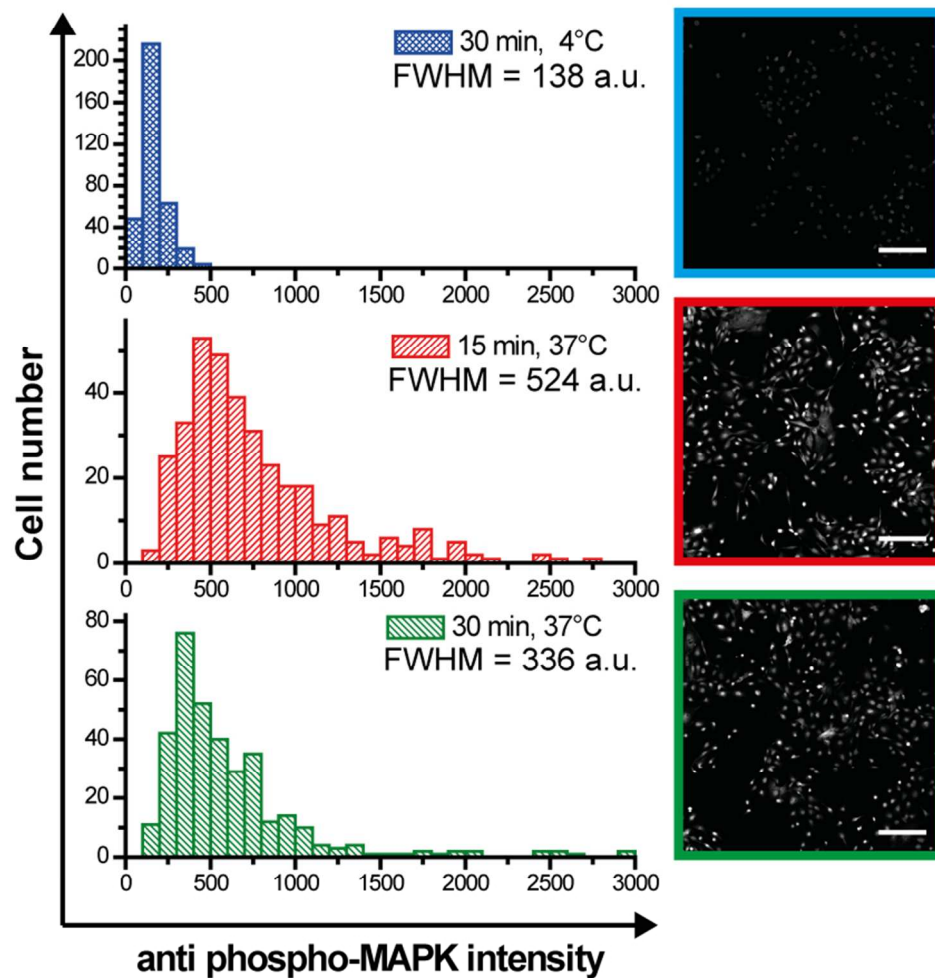


Figure 1. Cell-to-cell heterogeneity of HCC1143 breast cancer cells in their MAPK signaling response subsequent to EGF stimulation. | Each histogram was built from single-cell phospho-MAPK intensity levels (arbitrary units (a.u.)) from 3 independent experiments (9 confocal tiles per image, $N \geq 350$ cells per condition for each experiment). The Full width half maximum (FWHM) of the anti phospho-MAPK intensity is a measure of cellular heterogeneity. Typical micrographs are shown.

Fig. 1

76x80mm (300 x 300 DPI)

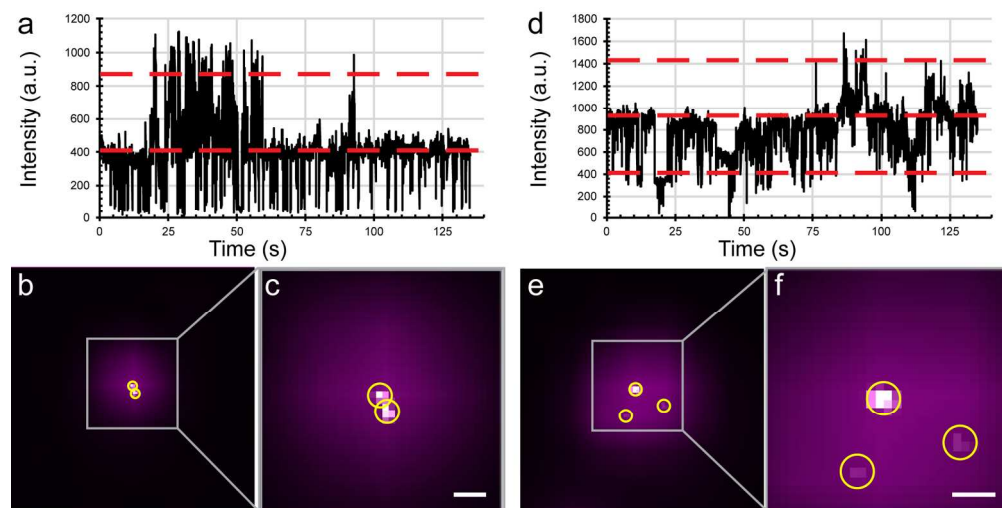


Figure 2. Super-resolution microscopy of EGFR clusters. | EBSQ bound to EGFR was imaged and super-resolved by gSHRImP based on QD blinking. A receptor dimer (A-C) or trimer (D-F) appears as a blurry spot expanding about 4-5 actual camera pixels (100nm/pixel) in diameter when imaged by diffraction-limited microscopy (purple). For visual guidance, we show the mean fluorescence intensity levels corresponding to the individual QDs by red dotted lines in QD blinking traces (A or D). Both traces have the background subtracted. The white overlay images in (B) and (E) represent the corresponding Gaussian point-spread-functions (PSFs) as determined via the gSHRImP algorithm. Please note that gSHRImP PSFs are not intensity-normalized. The final super-resolved images are generated by determining the centers of the single-molecule PSFs and are shown in zoomed-in micrographs in (C) for the dimer (EGFR molecules are 24nm apart) and (F) for the trimer (EGFR distances are 92nm, 107nm and 116nm, respectively). Yellow circles indicate individual EGFR molecule positions with the circle centers positioned at the calculated centroid positions of each EGFR molecule. Scale bars are 50nm.

Fig. 2

164x83mm (300 x 300 DPI)

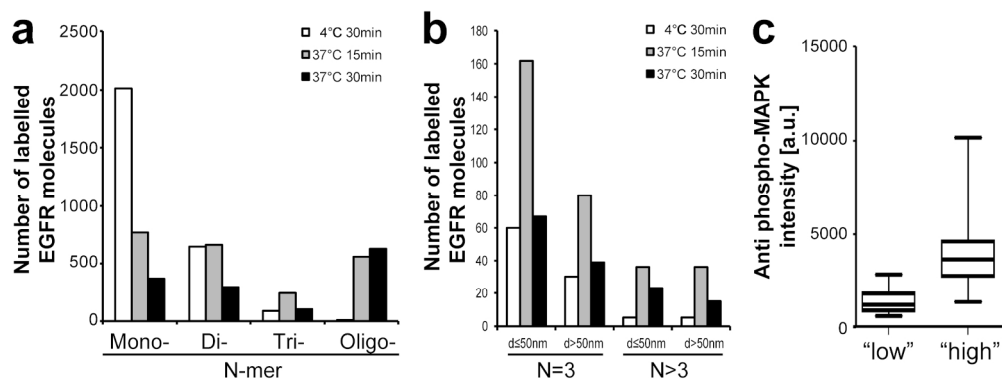


Figure 3. Cell-by-cell analysis of EGFR clusters. | (A) Number of resolved EGFR clusters under different treatment conditions. Clusters were categorized into EGFR monomers, dimers, trimers and oligomers as determined by counting the number of receptors per resolved cluster. Oligomers formed of more than 5-6 receptors could not always be resolved. (B) Trimers and fully resolvable multimers (i.e. clusters with $N=[4-6]$; from here onwards referred to as " $N>3$ " multimers) were analyzed for their intra-cluster distances between EGFR molecules. We categorized them as either $d \leq 50\text{nm}$ or $d > 50\text{nm}$. The relative numbers in those cluster categories change upon treatment. (C) Binary classification of each HCC1143 cell in each treatment condition into a "low" and "high" pMAPK intensity class. Data shown in all panels were obtained from 46 analyzed cells and 2164 clusters acquired in 2 independent experiments. The classes are significantly different; $P < 0.0001$ (unpaired two-tailed t -test with Welch's correction assuming unequal standard deviation).

Fig. 3

167x63mm (300 x 300 DPI)

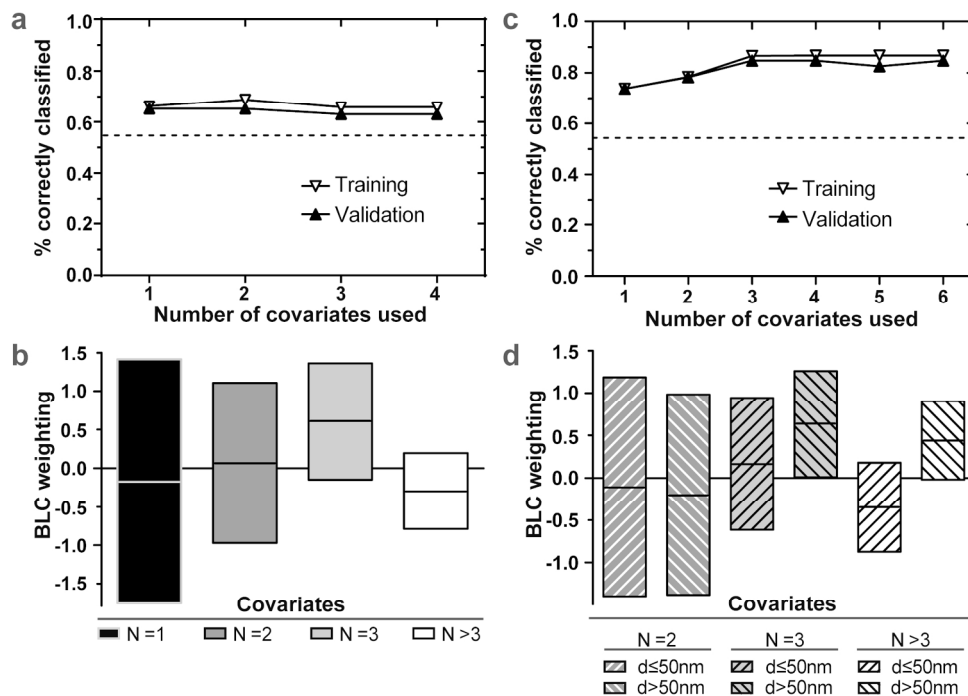


Figure 4. BLC-based prediction of cellular MAPK phosphorylation. | Prediction uses the number of EGFR molecules per cluster N as the only input parameter (A-B) or both N and the intra-cluster distances d as input parameters (C-D). (A/C) BLC prediction performance of the training and validation sets as a function of the number of covariates used. (B/D) Graphical representation of the regression weights assigned to each covariate. The magnitude of each weight gives a measure of how informative each covariate is in predicting the class membership. A positive weight implies that large values of that covariate are associated with the 'high' class whereas a negative weight indicates that large values of that covariate are associated with the 'low' class. The weights are obtained by averaging over the weights obtained during leave-one-out cross-validation with all covariates. The 95% confidence intervals of the regression weights are plotted. The Bayesian analysis has been performed on imaging data acquired in two independent experiments.

Fig. 4

165x115mm (300 x 300 DPI)

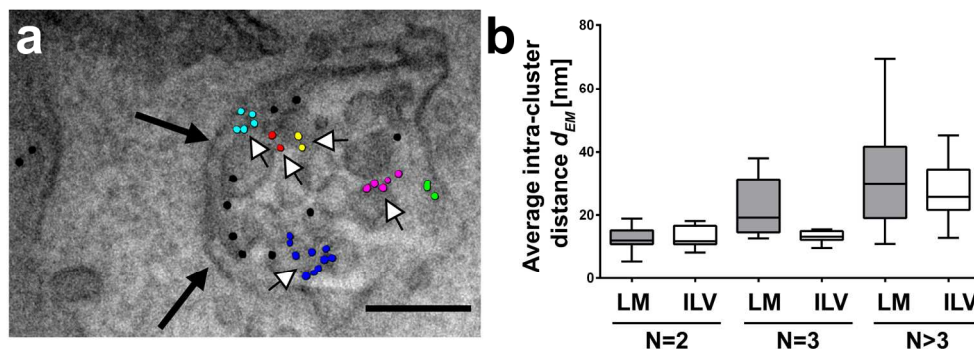


Figure 5. TEM analysis of EGFR clusters. | (A) Direct visualization and subcellular localization of EGF-induced EGFR cluster formation in HCC1143 cells. Black arrows point towards the limiting membrane of the MVB while white arrows point towards ILVs; scale bar is 100nm. (B) Partitioning between MVB limiting membranes or ILV membranes for dimers, trimers and multimers across all measured average intra-cluster distances; a box and whisker plot is shown with whiskers indicating minimum/maximum values. Localization on the limiting membrane of MVB becomes dominant with increasing average intra-cluster distance and number of receptors per cluster. Localization on the limiting membrane was found significantly different than localization on ILVs for trimers ($P=0.0247$) using unpaired two-tailed t -test with Welch's correction assuming unequal standard deviation.

Fig. 5

166x60mm (300 x 300 DPI)